Metal Transport by Magmatic Volatile Phases in Crustal Systems

Austin M. Gion[1,2*] and Fabrice Gaillard[1]

[1]Univ. Orléans, CNRS, BRGM, ISTO, UMR 7327, 1A Rue de la Férollerie – CS 20066, 45071 Orléans Cedex 2, France

[2]Department of Earth Science, University of Oxford, South Parks Road, Oxford OX1 3AN, United Kingdom

Keywords: Magmatic Volatile Phase, Magmatic-hydrothermal, metal transport

ABSTRACT

Magmatic volatile phases (MVPs) are multicomponent fluids that are a transport medium for metals being transferred from deep magmatic sources to sites of ore formation. However, the melt-to-fluid exchange of metals remains elusive because existing empirical simulations primarily address metal transport through the fate of one chemical element. In this study, we use a comprehensive thermochemical model to simulate the fractional crystallization of a silicate melt that degasses a multicomponent MVP. We show that the major and trace element abundances in MVPs formed from non-enriched magmatic systems are indistinguishable from MVPs found as fluid inclusions in mineralized and non-mineralized systems. We therefore conclude that ore formation is the consequence of repetitive intrusion-fractionation-degassing cycles common to crustal systems without pre-enriched sources, as opposed to scenarios wherein a particular or complex chemical system is required. Instead, the driving force of ore formation is a long-lived system fueled by a H_2O- and Cl-bearing melt. Variations in metal signatures of fluids therefore reflect the PT path of melt ascent and changes in major element composition of the melt.

INTRODUCTION

Magmatic-hydrothermal ore deposits host vast resources. Porphyry deposits alone produce 60-70% of the Cu, ~95% of the Mo, 80% of the Re, 20% of the Au, and almost all of the Te and Se worldwide (Sillitoe, 2010; John et al., 2016). The current paradigm for ore formation involves the concentration of metals in melts and fluids followed by the precipitation of ore minerals (Fig. 1). The sources of the metals and the mechanisms that can enrich or deplete melts are a topic of discussion and models generally invoke either: 1) Magmas that are pre-enriched in metals from the melting of previously enriched rocks or the scavenging of pre-existing sulfides (Core et al., 2006; Nadeau et al., 2010; Tang et al., 2020; Park et al., 2021; Holwell et al., 2022; Leong et al.,

2023; Markovic et al., 2025) or 2) Non-enriched sources which accumulate through time and/or have efficient metal extraction (Chiaradia and Caricchi, 2017; Lee and Tang, 2020; Chiaradia and Caricchi, 2022; Grondahl and Zajacz, 2022). Although a consensus has not been reached, it is clear that magmatic fluids play a vital role in the transport of metals (Hedenquist and Lowenstern, 1994; Audétat, 2019).

These fluids are known as magmatic volatile phases (MVP; Candela, 1997) and primarily comprise H_2O–CO_2 ± Cl ± F ± S (Hedenquist and Lowenstern, 1994; Tattitch et al., 2021) with variable major cation and trace metal contents. The exsolution of a MVP from the melt is due to either decompression (first boiling) or crystallization (second boiling; Candela, 1997). MVPs may be either intermediate-density fluids, low-salinity vapors, or high-salinity brines (Fig. 1). Depending on the bulk salinity and PT path, intermediate-density fluids may undergo phase separation resulting in co-existing vapor and brine (Bodnar et al., 1985; Driesner and Heinrich, 2007). The ascent of the MVP in the form of bubbles/plumes or channels is driven by their relatively high buoyancy and are a medium for metal transport (Candela, 1997; Degruyter et al., 2019). In order to assess potential metal sources, we used the model of Gion and Gaillard (2025), which considers the multicomponent exchange of major, minor, and trace elements between silicate melts, minerals, and aqueous fluids, to investigate the composition (44 elements) of MVPs formed from non-enriched magma sources and compare these fluids to fluid inclusions in barren and ore-bearing systems.

SIMULATION OF FLUID EVOLUTION IN THE CONTINENTAL CRUST

We simulated fractional crystallization of a melt by using the combined MELTS-FLUIDS software packages (Antoshechkina and Ghiorso, 2018; Gion and Gaillard, 2025), which calculates the composition of aqueous fluids at variable PTX conditions. The reader is referred to the

55 supplementary methods and Gion and Gaillard (2025) for details of MELTS-FLUIDS. We
56 performed two categories of modeling 1) Fractional crystallization of an average continental
57 andesites (Kelemen et al., 2007) along variable PT paths and varying volatile (H_2O and Cl)
58 contents and 2) Fractional crystallization of a melt with the composition of the upper continental
59 crust (UCC) (Rudnick and Gao, 2003). Initial trace element contents are those reported by
60 Kelemen et al. (2007) and Rudnick and Gao (2003) for their respective compositions. Some trace
61 elements (B, Ga, Mo, Cd, Tm) not provided by Kelemen et al. (2007) were set to bulk continental
62 crust values (Rudnick and Gao, 2003). The H_2O, Cl, and F content of each simulation ranged from
63 3.4 to 8, 0.3 to 0.5, and 0.01 to 0.05 grams per 100 grams of volatile-free melt, respectively. See
64 supplementary files for the bulk composition and crystal-melt partition coefficients used for each
65 simulation. All fluid-melt and brine-vapor equilibria were calculated as detailed in Gion and
66 Gaillard (2025) and bulk crystal-melt partition coefficients (supplementary files) were median
67 values taken from the GERM partition coefficient database (earthref.org) for relevant
68 combinations of melt compositions (andesites/dacites and rhyolites) and mineral phases. Note,
69 sulfide precipitation was not included due to limitations within MELTS. All simulations were
70 divided into three stages (Fig. 1). The first stage was isothermal decompression from 500 MPa to
71 the emplacement pressure (400-150 MPa) in 10 MPa steps at 970°C. This temperature is consistent
72 with the generation of intermediate to silicic melts (Annen et al., 2006) and the pressure is such
73 that the system is initially fluid undersaturated. The second stage was isobaric cooling from 970°C
74 to between 750 and 700°C in 10 or 25°C steps at the emplacement pressure. In isobaric and
75 isothermal regimes, the oxygen fugacity was fixed to QFM+1 (Quartz-Fayalite-Magnetite). In the
76 third stage a MVP that exsolved from the melt at its emplacement pressure (e.g. 200 MPa) is
77 decompressed and cooled along a PT path as suggested by Hemley and Hunt (1992). This

78 porphyry-forming stage takes place away from the melt in a rock-dominated system, but here we
79 focus only on the vapor-brine exchange of metals.

80 Figure 2 shows the results of a simulation for an andesite emplaced at 200 MPa. The results
81 of all other simulations are provided as supplementary files. During isothermal decompression the
82 melt becomes saturated with a supercritical fluid at 420 MPa (Fig. 2A). The major solutes in the
83 fluid are primarily (NaCl, $FeCl_2$)>($CaCl_2$, KCl) and the fluid contains moderate amounts (hundreds
84 to thousands of ppm) of other transition metals, e.g. Cu and Zn, as well as minor amounts (tens to
85 hundreds of ppm) of other alkali and alkaline earth metals, e.g. Ba, Rb, and Sr, and trace amounts
86 (hundreds of ppb to several ppm) of the REEs (Fig. 2B). During isobaric cooling the melt remains
87 saturated with a MVP and the major solutes are NaCl>($FeCl_2$, KCl, $CaCl_2$), as well as increasing
88 concentrations of most other elements as the melt crystalizes (Fig. 2B). The behavior of chlorine
89 (Supplementary Fig. S3) is consistent with previous experimental studies, wherein a calculated
90 $D_{Cl}^{Fluid/Melt}$ decreases with decreasing pressure (Tattitch et al., 2021).

91 During the porphyry-forming stage, phase separation occurs at 90 MPa and ~790°C. The
92 salinity of the vapor phase decreases with decreasing pressure and temperature, whereas the
93 salinity of the brine phase increases (Fig. 2C). The brine phase has higher concentrations of most
94 elements and contains thousands of ppm of Cu and Zn; hundreds of ppm of Ba and Sr; and tens of
95 ppm Rb and several ppm Li (Fig. 2C).

96 The variation of MVP compositions in wt% of solutes as a function of emplacement depth
97 and volatile content are shown in Fig. 2D. In an isothermal regime, fluids exsolved at higher
98 pressures are more saline and salinity decreases with decreasing pressure. In isobaric regimes, the
99 salinity of the fluids increases as temperature decreases and crystallization proceeds. Such results
100 are consistent with early exsolving fluids and fluids exsolving from evolved systems having the

highest salinity. The concentration of major elements in the fluid is directly correlated to the pressure of MVP exsolution and the salinity of the fluid. All major cations (Na, K, Ca, and Fe) decrease with decreasing salinity. However, Na is also higher, relative to K and Ca, in fluids that exsolve at higher pressures. Additionally, the major cation concentrations are directly related to the mineral phases, e.g. saturation with a spinel decreases Fe in the melt and thus limits Fe in the fluid. Finally, the trace element concentrations are higher in more saline fluids, but are affected by the timing of fluid exsolution and PT path of the melt (Fig 2D). It is also important to note that although drier melts produce fluids with roughly similar salinities and compositions, the amount of fluid produced is inherently smaller for similar sized melt bodies and thus limits mass transport of metals. Additionally, chlorine-rich melts do not necessarily produce higher salinity fluids (Fig 2D). This is because the salinity is controlled by the PT conditions at the time of fluid exsolution and the availability of cations such as Na, K, Ca, and Fe that exchange between the fluid and the melt (Gion and Gaillard, 2025). However, the presence of chlorine does promote the removal of metals from the melt and the transport of metals.

The compositions of the simulated supercritical fluids and coexisting vapor and brine phases are compared to natural fluid inclusions from a variety of granitic systems including Cu, Sn/W, and Mo deposits, as well as barren intrusions with compositionally similar fluids to economic deposits (Audétat, 2019; Fig. 3). The simulated MVPs are consistent with intermediate-density fluids (i.e. 5-15 wt% NaCl equiv.) in terms of both major and trace element concentrations. We observe that in the simulation performed with an andesitic melt and an emplacement pressure of 200 MPa, the concentrations of Na and K, as well as Li, Pb, and B are slightly lower than natural inclusions (Fig 3). However, emplacement at 400 MPa with the same initial bulk composition results in a MVP that more closely matches natural fluid inclusions for the major cations (Na, K,

Ca, and Fe) and some trace elements (Mo and Pb) (Fig 3). Thus, the composition of the fluid is greatly influenced by the PT path of the melt from which it exsolves. However, changing the PT path does not resolve the differences in Li and B compared to natural fluids. To resolve this, we consider a scenario where MVPs are exsolved from a magma with the initial bulk composition of the UCC. We chose this scenario to determine the composition of fluids that exsolve from more evolved melts. In this scenario the protracted fractionation results in a fluid that has a trace element signature that closely matches natural inclusions (Fig 3).

IMPLICATIONS AND CONCLUSIONS

The consistency between the simulated MVPs and natural fluid inclusions calls into question models that require pre-enriched sources for the formation of ore-deposits (Core et al., 2006; Nadeau et al., 2010; Tang et al., 2020; Park et al., 2021; Holwell et al., 2022; Leong et al., 2023). Because fluids derived from the fractional crystallization of a melt with an average andesitic composition or the average UCC contain equivalent metal concentrations as known ore-forming fluids, metal-rich sources are not necessary to produce potential ore-forming fluids. Instead, the primary control on fluid compositions is the major element composition of the melt and its evolution along various PT paths. Major elements (Na, K, Ca, Fe, etc.) are directly involved the fluid-melt exchange of both major and trace elements (Gion and Gaillard, 2025) and thus variation in melt composition, and the availability of such cations, influences the composition of exsolved fluids (Fig 3). Additionally, protracted crystallization and fluid exsolution results in trace elements (e.g. Li and B) that are consistent with natural inclusions. Therefore, the primary requirement for ore formation is a long-lived system fueled by a H_2O- and Cl-bearing melt, wherein MVPs transport metals to sites of deposition (e.g. Virmond et al., 2024). The model of Gion and Gaillard (2025) does not include sulfur-bearing species and thus our simulation lacks sulfur-complexed

147 metals. However, the presence of sulfur may increase the total metal load of a fluid (Tattitch and
148 Blundy, 2017). Thus, our results are consistent with sulfur being a secondary ligand (Fig. 3A) that
149 may not be required for the transportation of metals but is required for the precipitation of many
150 ore minerals (Holland, 1965; Blundy et al., 2015).

151 MVPs are also capable of transporting significant masses of elements that form gangue and
152 ore minerals. Assuming a magma injection rate of 10^{-3} km^3/yr (Caricchi et al., 2014) and an
153 average andesite composition (Kelemen et al., 2007) with 8, 0.3, and 0.05 grams of H_2O, Cl, and
154 F per 100 grams of volatile-free melt, respectively (Fig 2A-B; supplementary files), ~10^3 to 10^5
155 Mt of a MVP is exsolved from the melt in <2 Ma. This MVP transports 10^1 to 10^3 Mt of Fe, Na,
156 K, Ca and Cl, which are involved in the alteration of host rocks. We also find that the MVP
157 transports Cu, Zn, Pb, and Mo at masses equivalent to supergiant deposits on timescales of 0.1 to
158 2 Ma (Fig. 4); consistent with the previous observations of Chelle-Michou et al. (2017).

159 Our observations support metal-rich MVPs being derived from non-enriched magmatic
160 sources and highlight the potential for magmatic fluids as sources for a wide variety of metals.
161 Given these considerations, we conclude that ore formation is primarily a function of the total flux
162 of volatiles (Hogg et al., 2023). The total volatile flux depends on both the mass and volatile
163 content of the melt, wherein the total mass of H_2O and Cl exsolved form the melt must be sufficient
164 enough to transport several million tonnes of metals. The efficiency of such mass transport through
165 the transcrustal system is itself dependent on the lifespan of the system, timing of volatile
166 saturation, and fluid flow paths (Chiaradia and Caricchi, 2017; Audétat, 2019; Chelle-Michou and
167 Rottier, 2021; Chiaradia and Caricchi, 2022).

168

169

ACKNOWLEDGMENTS

This project has received funding through ANR grants ANR-10-LABX-100-01 (LabEx VOLTAIRE), ANR-11-EQPX-0036 (EquipEx PLANEX), ANR-18-CE31-0021 (GASTON), ANR-24-CE49-6543 (MAGBRINES), as well as from the European Union's Horizon Europe research and innovation program under grant agreement number 101166936 (GEOASTRONOMY). The authors are grateful for the advice from Michel Pichavant, Phil Piccoli, Phil Candela, Andrea Carolina Ojeda-Porras, Bence Horányi, and Jon Blundy. We thank Cyril Chelle-Michou, Lucca Caricchi, and two anonymous reviewers for their constructive feedback.

Supplemental Material. Supplemental information contains additional figures detailing the results of the simulation, as well as the input and output files of the model. Please visit https://doi.org/10.1130/XXXX to access the supplemental material and contact editing@geosociety.org with any questions.

Figure Captions

Fig. 1: Schematic cross section of a transcrustal magmatic system after Chelle-Michou and Rottier (2021). Fluid saturation and phase separation are marked by the dashed lines. Blue arrows illustrate the three stages of the simulations. PT plot is a simulation for fractional crystallization an average continental andesite with the mass fraction of phases in the system and the distribution of Cu and Zn among those phases.

Fig. 2: Stacked area plots of simulation results for an average hydrous continental andesite. **A)** Composition of simulated supercritical fluid during isothermal decompression. **B)** Composition of simulated supercritical fluid isobaric cooling. **C)** Composition of vapor and brine during decompression and cooling of the supercritical fluid. The left-hand axis is the concentration in wt%. The inset values are the concentrations of grouped elements in ppm (bold, italic font) or ppb (regular font) at the beginning and end of each stage. The right-hand axis is $\log_{10} X_{HCl}^{Fluid}$ and $\log_{10} X_{HF}^{Fluid}$. REE = Rare Earth Elements + Th + U. AA = Minor Alkali and Alkaline Earth Metals. TM = Minor Transition Metals + Post-transition Metals + Metalloids. **D)** Comparisons of supercritical fluids exsolved from andesitic melts with variable emplacement pressures, water, and chlorine (grams per 100 grams of anhydrous melt) contents. Isothermal decompression and isobaric cooling are denoted by a star and circle, respectively.

Fig. 3: Comparison of simulated MVPs exsolved from an andesite emplaced at 200 MPa and 400 MPa, as well as MVPs exsolved from the upper continental crust to natural fluid inclusions from Audétat (2019) for ore-deposits and barren intrusion. **A)** Simulated supercritical fluids compared to natural intermediate-density fluid inclusions. **B)** Simulated low-salinity vapors compared to natural intermediate-density fluid inclusions; the database of Audétat (2019) does not include low-salinity vapors. **C)** Simulated brines compared to natural brines. Violins are natural fluids.

208 Note, the andesite emplaced at 400 MPa never enters a two-phase field. Each data point
209 represents one PT step.
210 **Fig. 4:** Mass of elements transported and mass of degassed MVP (supercritical fluid or vapor +
211 brine) in million tonnes (Mt) vs time (Ma) calculated using the MVP compositions in Fig 2A-B
212 and assuming a magma injection rate of 10^{-3} km^3/yr (Chiaradia and Caricchi, 2022). Colored
213 regions are determined by the thresholds (and subdivisions) of large, giant, and supergiant
214 deposits as defined by Laznicka (2014) for a given metal, as well as the time required to
215 transport an equivalent mass, i.e. mass of metal to cross a deposit size threshold, of that metal by
216 the simulated MVP; the mass of the MVP, Cl, Fe, Na, and K were not used to define these fields.

References

Annen, C., Blundy, J. D., and Sparks, R. S. J., 2006, The Genesis of Intermediate and Silicic Magmas in Deep Crustal Hot Zones: Journal of Petrology, v. 47, no. 3, p. 505-539, doi:10.1093/petrology/egi084.

Antoshechkina, P. M., and Ghiorso, M. S., 2018, MELTS for MATLAB: A new educational and research tool for computational thermodynamics, Volume 2018, p. ED44B-23.

Audétat, A., 2019, The metal content of magmatic-hydrothermal fluids and its relationship to mineralization potential: Economic Geology, v. 114, no. 6, p. 1033-1056, doi:10.5382/econgeo.4673.

Blundy, J., Mavrogenes, J., Tattitch, B., Sparks, S., and Gilmer, A., 2015, Generation of porphyry copper deposits by gas–brine reaction in volcanic arcs: Nature Geoscience, v. 8, no. 3, p. 235-240, doi:10.1038/ngeo2351.

Bodnar, R. J., Burnham, C. W., and Sterner, S. M., 1985, Synthetic fluid inclusions in natural quartz. III. Determination of phase equilibrium properties in the system H_2O-NaCl to 1000°C and 1500 bars: Geochimica et Cosmochimica Acta, v. 49, no. 9, p. 1861-1873, doi:10.1016/0016-7037(85)90081-X.

Candela, P. A., 1997, A review of shallow, ore-related granites: textures, volatiles, and ore metals: Journal of Petrology, v. 38, no. 12, p. 1619-1633, doi:10.1093/petroj/38.12.1619.

Caricchi, L., Simpson, G., and Schaltegger, U., 2014, Zircons reveal magma fluxes in the Earth's crust: Nature, v. 511, no. 7510, p. 457-461, doi:10.1038/nature13532.

Chelle-Michou, C., and Rottier, B., 2021, Transcrustal magmatic controls on the size of porphyry Cu systems: State of knowledge and open questions, Tectonomagmatic Influences on Metallogeny and Hydrothermal Ore Deposits: A Tribute to Jeremy P. Richards (Volume I), Volume SP 24 vol. 1, Society of Economic Geologists, p. 0.

Chelle-Michou, C., Rottier, B., Caricchi, L., and Simpson, G., 2017, Tempo of magma degassing and the genesis of porphyry copper deposits: Scientific Reports, v. 7, no. 1, p. 40566, doi:10.1038/srep40566.

Chiaradia, M., and Caricchi, L., 2017, Stochastic modelling of deep magmatic controls on porphyry copper deposit endowment: Scientific Reports, v. 7, no. 1, p. 44523, doi:10.1038/srep44523.

Chiaradia, M., and Caricchi, L., 2022, Supergiant porphyry copper deposits are failed large eruptions: Communications Earth & Environment, v. 3, no. 1, p. 107, doi:10.1038/s43247-022-00440-7.

Core, D. P., Kesler, S. E., and Essene, E. J., 2006, Unusually Cu-rich magmas associated with giant porphyry copper deposits: Evidence from Bingham, Utah: Geology, v. 34, no. 1, p. 41-44, doi:10.1130/g21813.1.

Degruyter, W., Parmigiani, A., Huber, C., and Bachmann, O., 2019, How do volatiles escape their shallow magmatic hearth?: Philosophical Transactions of the Royal Society A: Mathematical, Physical and Engineering Sciences, v. 377, no. 2139, p. 20180017, doi:doi:10.1098/rsta.2018.0017.

Driesner, T., and Heinrich, C. A., 2007, The system H_2O–NaCl. Part I: Correlation formulae for phase relations in temperature–pressure–composition space from 0 to 1000°C, 0 to 5000bar, and 0 to 1 X_{NaCl}: Geochimica et Cosmochimica Acta, v. 71, no. 20, p. 4880-4901, doi:10.1016/j.gca.2006.01.033.

Gion, A. M., and Gaillard, F., 2025, The multicomponent exchange of metals between magmatic fluids and silicate melts: Geochimica et Cosmochimica Acta, v. 395, p. 112-134, doi:10.1016/j.gca.2025.01.033.
Grondahl, C., and Zajacz, Z., 2022, Sulfur and chlorine budgets control the ore fertility of arc magmas: Nature Communications, v. 13, no. 1, p. 4218, doi:10.1038/s41467-022-31894-0.
Hedenquist, J. W., and Lowenstern, J. B., 1994, The role of magmas in the formation of hydrothermal ore deposits: Nature, v. 370, no. 6490, p. 519-527.
Hemley, J. J., and Hunt, J. P., 1992, Hydrothermal ore-forming processes in the light of studies in rock-buffered systems; II, Some general geologic applications: Economic Geology, v. 87, no. 1, p. 23-43, doi:10.2113/gsecongeo.87.1.23.
Hogg, O. R., Edmonds, M., and Blundy, J., 2023, Water-rich magmas optimise volcanic chalcophile element outgassing fluxes: Earth and Planetary Science Letters, v. 611, p. 118153, doi:10.1016/j.epsl.2023.118153.
Holland, H. D., 1965, Some applications of thermochemical data to problems of ore deposits; [Part] 2, Mineral assemblages and the composition of ore forming fluids: Economic Geology, v. 60, no. 6, p. 1101-1166, doi:10.2113/gsecongeo.60.6.1101.
Holwell, D. A., Fiorentini, M. L., Knott, T. R., McDonald, I., Blanks, D. E., Campbell McCuaig, T., and Gorczyk, W., 2022, Mobilisation of deep crustal sulfide melts as a first order control on upper lithospheric metallogeny: Nature Communications, v. 13, no. 1, p. 573, doi:10.1038/s41467-022-28275-y.
John, D. A., Taylor, R. D., Verplanck, P. L., and Hitzman, M. W., 2016, By-products of porphyry copper and molybdenum deposits, Rare Earth and Critical Elements in Ore Deposits, Volume 18, Society of Economic Geologists, p. 0.
Kelemen, P. B., Hanghøj, K., and Greene, A. R., 2007, 3.18 - One View of the Geochemistry of Subduction-Related Magmatic Arcs, with an Emphasis on Primitive Andesite and Lower Crust, *in* Holland, H. D., and Turekian, K. K., eds., Treatise on Geochemistry: Oxford, Pergamon, p. 1-70.
Laznicka, P., 2014, Giant metallic deposits—A century of progress: Ore Geology Reviews, v. 62, p. 259-314, doi:10.1016/j.oregeorev.2014.03.002.
Lee, C.-T. A., and Tang, M., 2020, How to make porphyry copper deposits: Earth and Planetary Science Letters, v. 529, p. 115868, doi:10.1016/j.epsl.2019.115868.
Leong, T. S. J., Mavrogenes, J. A., and Arculus, R. J., 2023, Water-sulfur-rich, oxidised adakite magmas are likely porphyry copper progenitors: Scientific Reports, v. 13, no. 1, p. 5078, doi:10.1038/s41598-023-31736-z.
Markovic, S., Szymanowski, D., Tavazzani, L., Torró, L., Kouzmanov, K., Kalinaj, M., and Chelle-Michou, C., 2025, Timescales of magmatic-hydrothermal activity at the giant San Rafael tin deposit (Peru): Earth and Planetary Science Letters, v. 671, p. 119624, doi:10.1016/j.epsl.2025.119624.
Nadeau, O., Williams-Jones, A. E., and Stix, J., 2010, Sulphide magma as a source of metals in arc-related magmatic hydrothermal ore fluids: Nature Geoscience, v. 3, no. 7, p. 501-505, doi:10.1038/ngeo899.
Park, J.-W., Campbell, I. H., Chiaradia, M., Hao, H., and Lee, C.-T., 2021, Crustal magmatic controls on the formation of porphyry copper deposits: Nature Reviews Earth & Environment, v. 2, no. 8, p. 542-557, doi:10.1038/s43017-021-00182-8.

Rudnick, R. L., and Gao, S., 2003, Composition of the continental crust, *in* Holland, H. D., and Turekian, K. K., eds., Treatise on Geochemistry: Oxford, Pergamon, p. 1-64.
Sillitoe, R. H., 2010, Porphyry copper systems: Economic Geology, v. 105, no. 1, p. 3-41, doi:10.2113/gsecongeo.105.1.3.
Tang, M., Lee, C.-T. A., Ji, W.-Q., Wang, R., and Costin, G., 2020, Crustal thickening and endogenic oxidation of magmatic sulfur: Science Advances, v. 6, no. 31, p. eaba6342, doi:doi:10.1126/sciadv.aba6342.
Tattitch, B., Chelle-Michou, C., Blundy, J., and Loucks, R. R., 2021, Chemical feedbacks during magma degassing control chlorine partitioning and metal extraction in volcanic arcs: Nature Communications, v. 12, no. 1, p. 1774, doi:10.1038/s41467-021-21887-w.
Tattitch, B. C., and Blundy, J. D., 2017, Cu-Mo partitioning between felsic melts and saline-aqueous fluids as a function of X_{NaCleq}, f_{O2}, and f_{S2}: American Mineralogist, v. 102, no. 10, p. 1987-2006, doi:10.2138/am-2017-5998.
Virmond, A. L., Wotzlaw, J.-F., Rojas-Arancibia, R., Selby, D., and Chelle-Michou, C., 2024, Multi-million-year magmatic and hydrothermal activity is key to the formation of supergiant to behemothian porphyry copper deposits: Contributions to Mineralogy and Petrology, v. 179, no. 10, p. 88, doi:10.1007/s00410-024-02167-4.

325

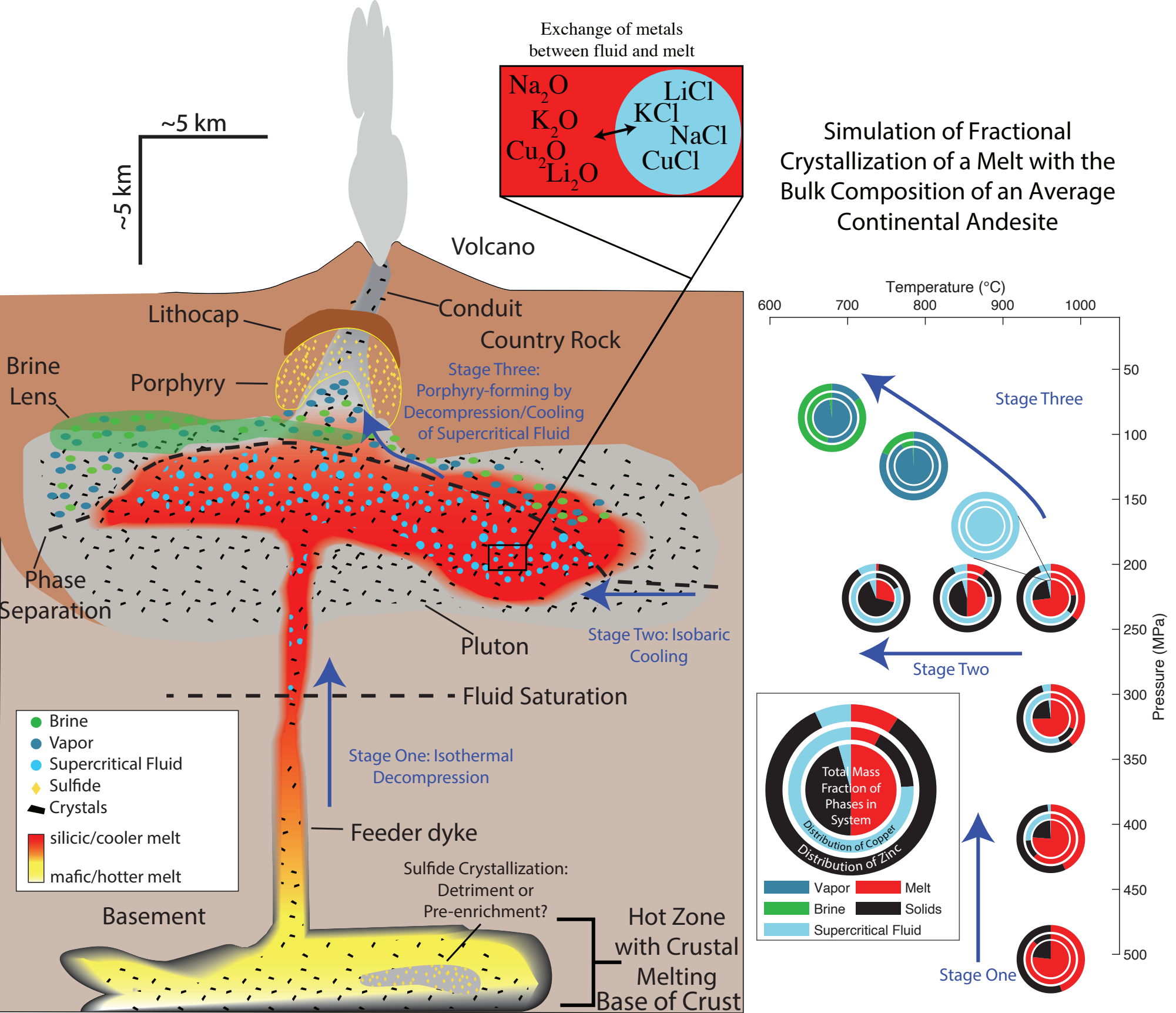
Exchange of metals between fluid and melt
Na_2O
K_2O
Cu_2O
Li_2O
LiCl
KCl
NaCl
CuCl
~5 km
~5 km
Volcano
Lithocap
Conduit
Country Rock
Brine Lens
Porphyry
Stage Three: Porphyry-forming by Decompression/Cooling of Supercritical Fluid
Phase Separation
Pluton
Stage Two: Isobaric Cooling
Fluid Saturation
Stage One: Isothermal Decompression
Feeder dyke
Brine
Vapor
Supercritical Fluid
Sulfide
Crystals
silicic/cooler melt
mafic/hotter melt
Basement
Sulfide Crystallization: Detriment or Pre-enrichment?
Hot Zone with Crustal Melting
Base of Crust
Simulation of Fractional Crystallization of a Melt with the Bulk Composition of an Average Continental Andesite
Temperature (°C)
600
700
800
900
1000
Pressure (MPa)
50
100
150
200
250
300
350
400
450
500
Stage Three
Stage Two
Stage One
Total Mass Fraction of Phases in System
Distribution of Copper
Distribution of Zinc
Vapor
Melt
Brine
Solids
Supercritical Fluid

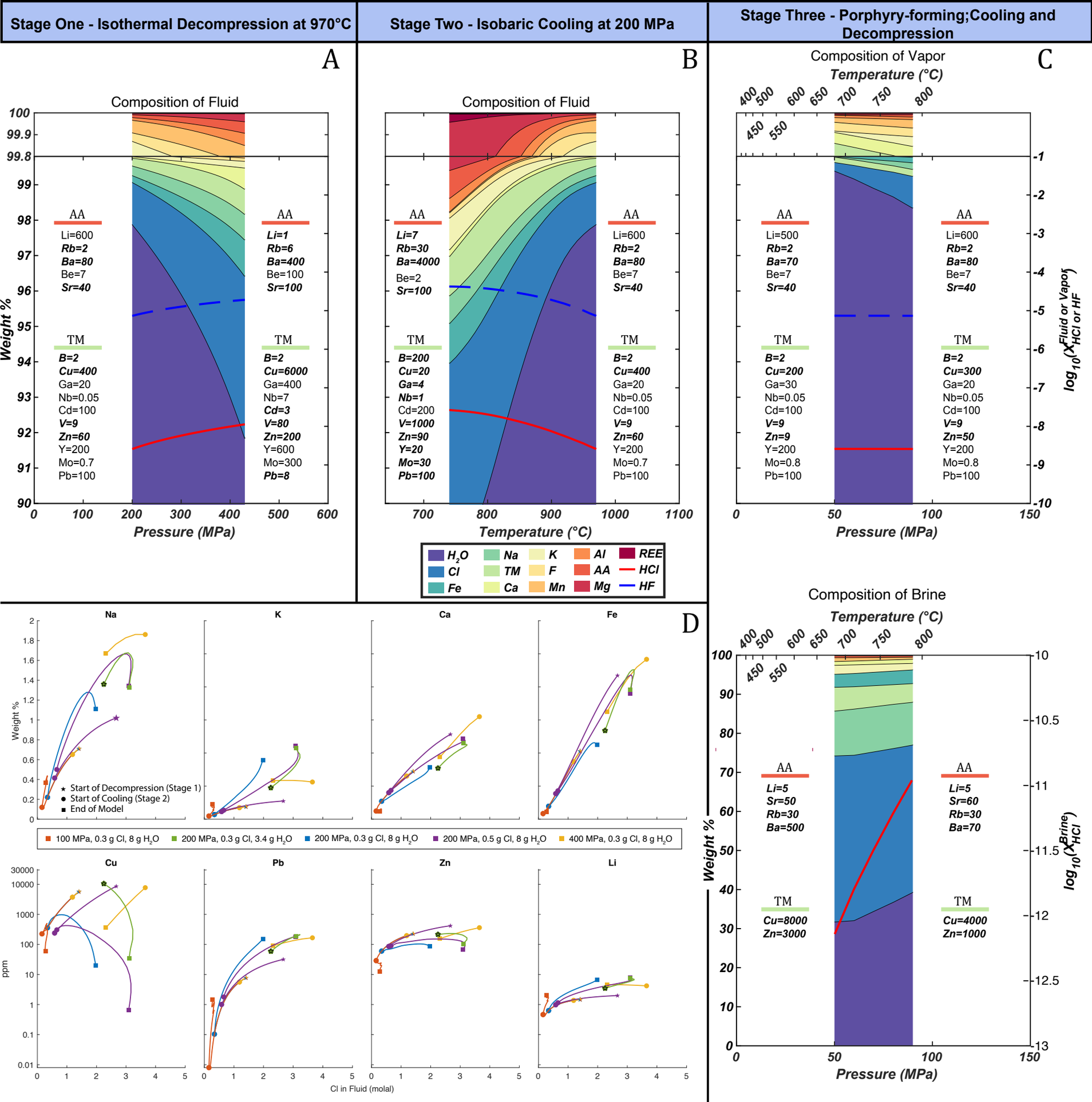
Stage One - Isothermal Decompression at 970°C
Stage Two - Isobaric Cooling at 200 MPa
Stage Three - Porphyry-forming;Cooling and Decompression
A
B
C
D
Composition of Fluid
Composition of Fluid
Composition of Vapor
Temperature (°C)
Weight %
Pressure (MPa)
Temperature (°C)
$log_{10}(X^{Fluid\ or\ Vapor}_{HCl\ or\ HF})$
AA
Li=600
Rb=2
Ba=80
Be=7
Sr=40
TM
B=2
Cu=400
Ga=20
Nb=0.05
Cd=100
V=9
Zn=60
Y=200
Mo=0.7
Pb=100
AA
Li=1
Rb=6
Ba=400
Be=100
Sr=100
TM
B=2
Cu=6000
Ga=400
Nb=7
Cd=3
V=80
Zn=200
Y=600
Mo=300
Pb=8
AA
Li=7
Rb=30
Ba=4000
Be=2
Sr=100
TM
B=200
Cu=20
Ga=4
Nb=1
Cd=200
V=1000
Zn=90
Y=20
Mo=30
Pb=100
AA
Li=600
Rb=2
Ba=80
Be=7
Sr=40
TM
B=2
Cu=400
Ga=20
Nb=0.05
Cd=100
V=9
Zn=60
Y=200
Mo=0.7
Pb=100
AA
Li=500
Rb=2
Ba=70
Be=7
Sr=40
TM
B=2
Cu=200
Ga=30
Nb=0.05
Cd=100
V=9
Zn=9
Y=200
Mo=0.8
Pb=100
AA
Li=600
Rb=2
Ba=80
Be=7
Sr=40
TM
B=2
Cu=300
Ga=20
Nb=0.05
Cd=100
V=9
Zn=50
Y=200
Mo=0.8
Pb=100
H_2O
Cl
Fe
Na
TM
Ca
K
F
Mn
Al
AA
Mg
REE
HCl
HF
Na
K
Ca
Fe
Weight %
Start of Decompression (Stage 1)
Start of Cooling (Stage 2)
End of Model
100 MPa, 0.3 g Cl, 8 g H_2O
200 MPa, 0.3 g Cl, 3.4 g H_2O
200 MPa, 0.3 g Cl, 8 g H_2O
200 MPa, 0.5 g Cl, 8 g H_2O
400 MPa, 0.3 g Cl, 8 g H_2O
Cu
Pb
Zn
Li
ppm
Cl in Fluid (molal)
Composition of Brine
Temperature (°C)
Weight %
Pressure (MPa)
$log_{10}(X^{Brine}_{HCl})$
AA
Li=5
Sr=50
Rb=30
Ba=500
TM
Cu=8000
Zn=3000
AA
Li=5
Sr=60
Rb=30
Ba=70
TM
Cu=4000
Zn=1000

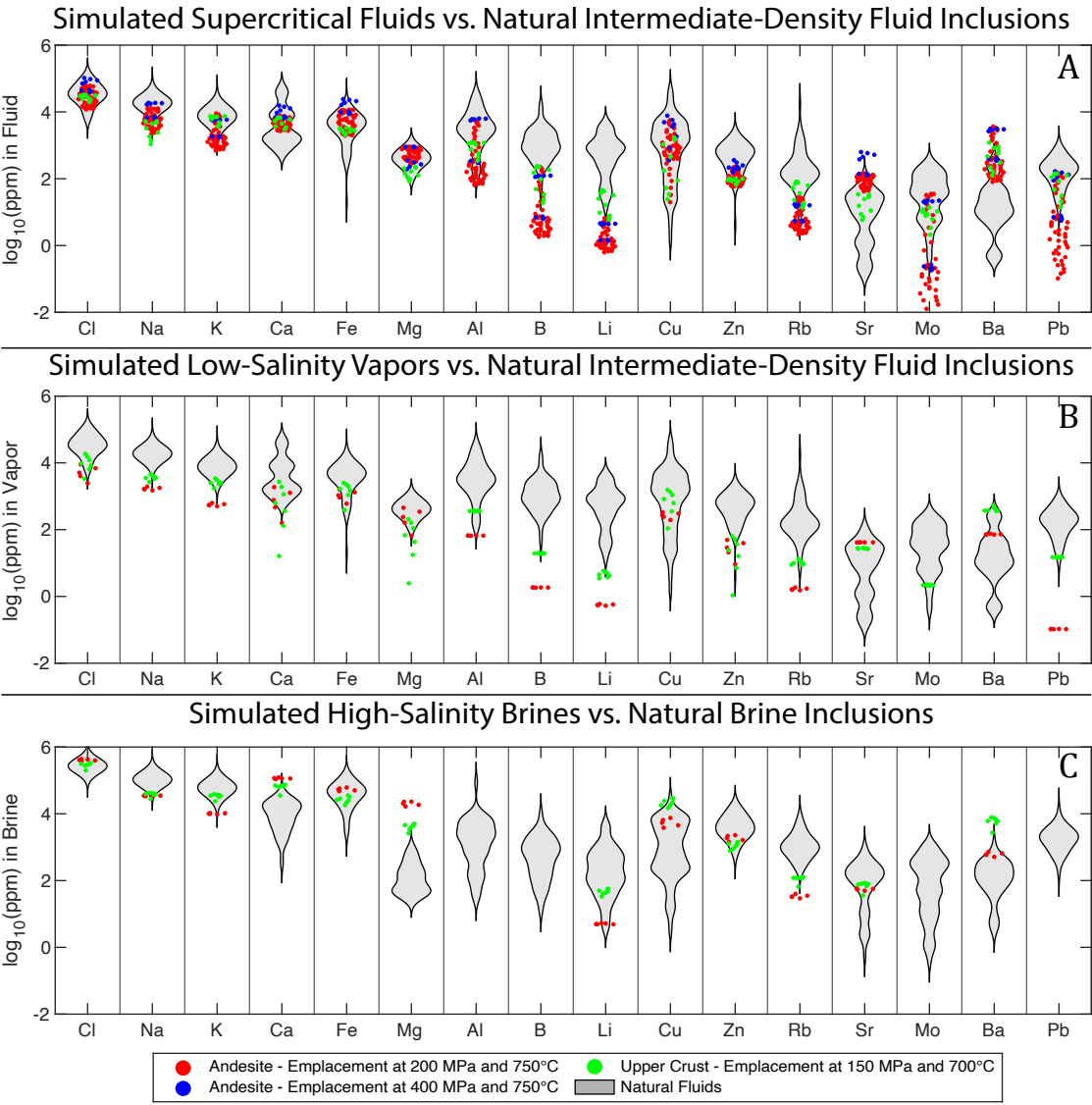
Simulated Supercritical Fluids vs. Natural Intermediate-Density Fluid Inclusions
A
log10(ppm) in Fluid
6
4
2
0
-2
Cl
Na
K
Ca
Fe
Mg
Al
B
Li
Cu
Zn
Rb
Sr
Mo
Ba
Pb
Simulated Low-Salinity Vapors vs. Natural Intermediate-Density Fluid Inclusions
B
log10(ppm) in Vapor
Simulated High-Salinity Brines vs. Natural Brine Inclusions
C
log10(ppm) in Brine
Andesite - Emplacement at 200 MPa and 750°C
Andesite - Emplacement at 400 MPa and 750°C
Upper Crust - Emplacement at 150 MPa and 700°C
Natural Fluids

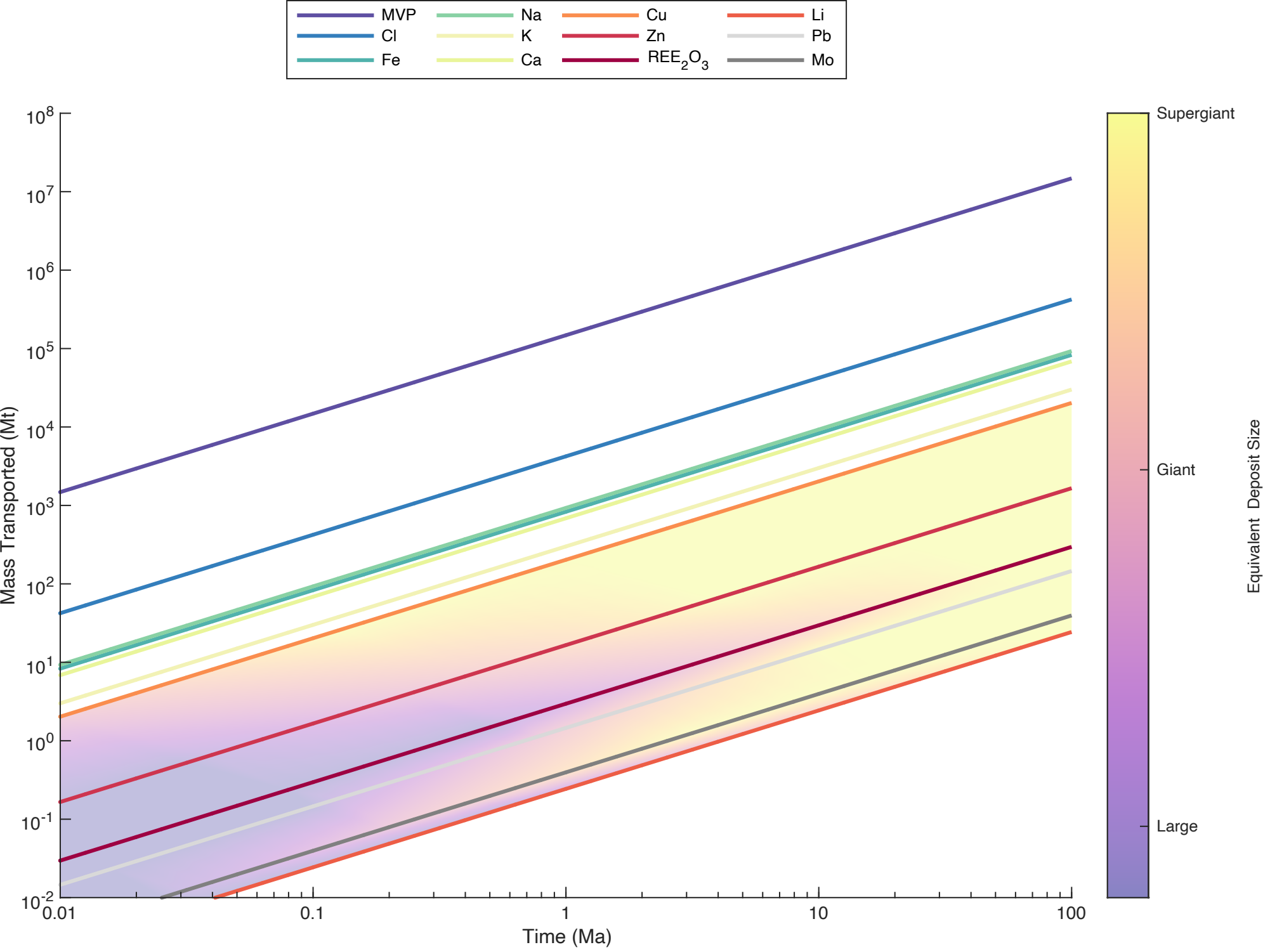
MVP
Cl
Fe
Na
K
Ca
Cu
Zn
REE2O3
Li
Pb
Mo
Mass Transported (Mt)
Time (Ma)
Equivalent Deposit Size
Supergiant
Giant
Large